AGU PUBLICATIONS

JGR

Journal of Geophysical Research: Space Physics

RESEARCH ARTICLE

10.1002/2014JA019863

Key Points:
- Current loops in substorm current wedge identified from magnetic perturbations
- Substorm current wedge includes both region 1 and region 2
- Current closure identified at ionospheric proxy

Correspondence to:
J. Birn,
jbirn@spacescience.org

Citation:
Birn, J., and M. Hesse (2014), The substorm current wedge: Further insights from MHD simulations, *J. Geophys. Res. Space Physics*, *119*, 3503–3513, doi:10.1002/2014JA019863.

Received 18 FEB 2014
Accepted 21 APR 2014
Accepted article online 24 APR 2014
Published online 15 MAY 2014

The substorm current wedge: Further insights from MHD simulations

J. Birn[1,2] and M. Hesse[3]

[1]Space Science Institute, Boulder, Colorado, USA, [2]Los Alamos National Laboratory, Los Alamos, New Mexico, USA, [3]NASA/Goddard Space Flight Center, Greenbelt, Maryland, USA

Abstract Using a recent magnetohydrodynamic simulation of magnetotail dynamics, we further investigate the buildup and evolution of the substorm current wedge (SCW), resulting from flow bursts generated by near-tail reconnection. Each flow burst generates an individual current wedge, which includes the reduction of cross-tail current and the diversion to region 1 (R1)-type field-aligned currents (earthward on the dawn and tailward on the duskside), connecting the tail with the ionosphere. Multiple flow bursts generate initially multiple SCW patterns, which at later times combine to a wider single SCW pattern. The standard SCW model is modified by the addition of several current loops, related to particular magnetic field changes: the increase of B_z in a local equatorial region (dipolarization), the decrease of $|B_x|$ away from the equator (current disruption), and increases in $|B_y|$ resulting from azimuthally deflected flows. The associated loop currents are found to be of similar magnitude, 0.1–0.3 MA. The combined effect requires the addition of region 2 (R2)-type currents closing in the near tail through dawnward currents but also connecting radially with the R1 currents. The current closure at the inner boundary, taken as a crude proxy of an idealized ionosphere, demonstrates westward currents as postulated in the original SCW picture as well as North-South currents connecting R1- and R2-type currents, which were larger than the westward currents by a factor of almost 2. However, this result should be applied with caution to the ionosphere because of our neglect of finite resistance and Hall effects.

1. Introduction

The substorm current wedge (SCW) [*McPherron et al.*, 1973] constitutes the main paradigm of magnetotail-ionosphere interaction associated not only with substorms but also with earthward flow burst events that do not lead to full substorms [e.g., *Henderson et al.*, 1998; *Sergeev et al.*, 1999; *Lyons et al.*, 1999; *Nakamura et al.*, 2001a, 2001b]. Its major component consists of a reduction of the cross-tail current in a central tail section, associated with a collapse and dipolarization of magnetic field, combined with a deviation of current to the ionosphere, where it closes through the westward auroral electrojet. This simple current loop involves field-aligned currents connecting magnetotail and ionosphere with the sense of "region 1" (R1) [*Iijima and Potemra*, 1976], that is, earthward on the dawnside and tailward on the duskside.

In a recent paper [*Birn and Hesse*, 2013] we used magnetohydrodynamic (MHD) simulations to demonstrate the buildup of the field-aligned current system by flow bursts or "flow channels," shearing, or twisting the magnetic field. These simulations also showed the relevance of close penetration of the flows in the buildup, the incorporation of an additional, region 2 (R2) type, current system, and the possibility of multiple flow bursts leading to an accumulation of dipolarized flux tubes.

Using the same MHD simulation of near-tail reconnection [*Birn et al.*, 2011], we here illustrate further properties of the current wedge picture, focusing in particular on the different current systems and their evolution. The description of the SCW, or any current system, by some number of current loops appears somewhat arbitrary. Here we demonstrate that a natural way of identifying major current systems can be associated with the main changes in the magnetic field components. Major properties of the MHD simulation are described by *Birn et al.* [2011] and *Birn and Hesse* [2013] and will not be repeated here. Here we just note that the simulation was based on dimensionless quantities with suitable units given by

$$L_n = 10,000\,\text{km} \approx 1.5\,R_E, \quad B_n = 20\,\text{nT}, \quad v_n = 1,000\,\text{km/s} \tag{1}$$

This leads to derived units $t_n = L_n/v_n = 10\,\text{s}$, $p_n = B_n^2/\mu_0 = 0.32\,\text{nP}$, $j_n = B_n/(\mu_0 L_n) = 1.6\,\text{nA/m}^2$, and $I_n = B_n L_n/\mu_0 = 0.16\,\text{MA}$. The simulation box spans the region $-7.5\,R_E > x > -97.5\,R_E$, $|z| < 15\,R_E$,

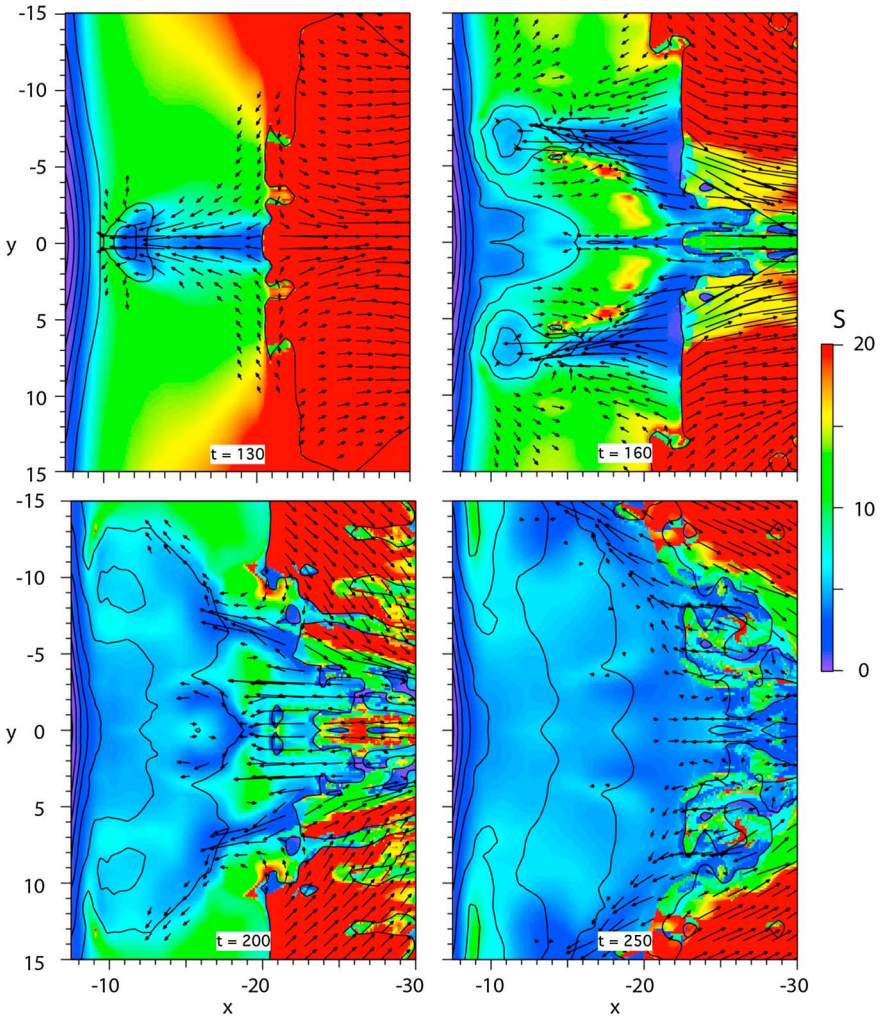

Figure 1. Entropy function $S = \int p^{1/\gamma} ds/B$ (color) and flow vectors in the x, y plane at three different times, for a simulation of near-tail reconnection, modified after Figure 6 of *Birn and Hesse* [2013]. Solid black lines represent contours of constant B_z, shown at intervals of 0.5 (10 nT); the one farthest to the right represents the $B_z = 0$ line.

$|y| < 60\ R_E$. (The extent in y was unusually wide for comparison with a simulation with strong cross-tail magnetic field, which is not relevant here.) The initial state consisted of a tail field with a superposed dipole with a center located at $x = 0$ outside the simulation box. The evolution included a relaxation phase ($0 < t < 30$, corresponding to 300 s), during which the system relaxed into full equilibrium [*Hesse and Birn*, 1993], followed by a driven phase ($30 < t < 61$), during which an external inflow of magnetic flux was applied to the top and bottom boundaries. This leads to current intensification and the formation of a thin embedded current sheet. At $t = 61$ finite resistivity was imposed, concentrated in the region of enhanced current density, which caused the onset of reconnection and the formation of a neutral line ($B_z = 0$) at $t \approx 90$.

A main property of interest for the present paper is the fact that the simulation consisted not only of an initial flow burst near midnight, starting around $t = 125$, but also of additional flow bursts off midnight delayed by a few minutes. These flow bursts and their association with entropy-depleted magnetic flux tubes are illustrated in Figure 1, modified and extended after *Birn and Hesse* [2013]. Here the color-coded function S denotes an entropy measure defined by

$$S = \int p^{1/\gamma} ds/B \qquad \text{with} \quad \gamma = 5/3 \tag{2}$$

integrated along field lines from one boundary crossing point to another [*Birn et al.*, 2009; *Wolf et al.*, 2009]. For closed field lines of interest here the crossing points are at the near-Earth boundary. (For plasmoid field lines, identified by several crossings of the $z = 0$ plane, the integral was taken over one loop, from one

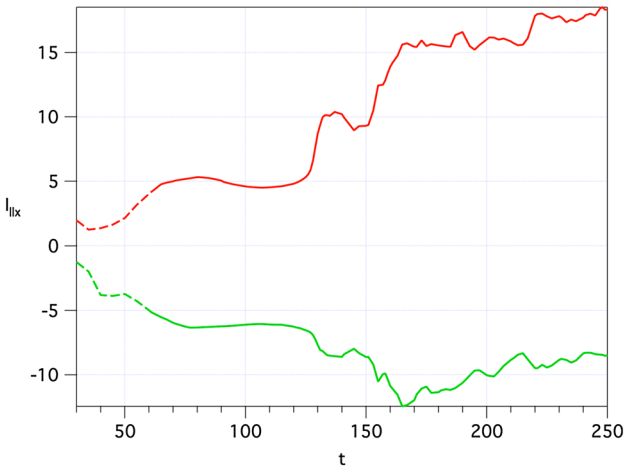

Figure 2. Evolution of the total current of region 1 (positive, red curve) and region 2 signature (negative, green curve), integrated for $y < 0, z > 0$ within the closed field line region. The current unit corresponds to 0.16 MA.

equatorial crossing to another.) Solid black lines represent contours of constant B_z, shown at intervals of 10 nT; the one farthest to the right represents the $B_z = 0$ line. The closed contours at the front of each flow burst indicate the dipolarization fronts. Black arrows show velocity vectors with a speed above 100 km/s.

At $t = 130$, Figure 1 shows a single flow burst near midnight, associated with a region of reduced entropy originating from the reconnection site. The velocity vectors demonstrate not only the earthward flow bursts but also flow vortices surrounding the dipolarization front. At $t = 160$ the central flow burst has largely subsided, leaving a region of enhanced B_z and reduced S near the dipolar region, while additional flow bursts near $y = \pm 7$ can be seen, each associated with their individual low-entropy, high-B_z regions, and vorticity patterns. At $t = 200$ these flow bursts have been deflected and slowed, while additional flows within $|y| \lesssim 3$ add to the dipolarization near midnight. Finally, at $t = 250$ the near-Earth flows have largely subsided and left a wide accumulation of low-entropy, high-B_z regions.

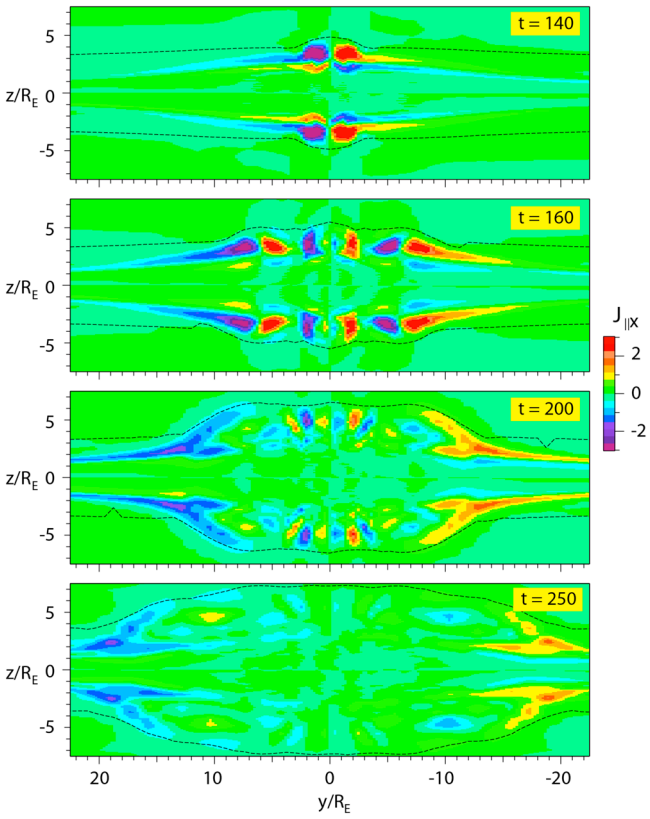

Figure 3. Color-coded field-aligned current component $j_{\|x}$ at the inner boundary for various times as indicated. The dashed lines show the open-closed field line boundaries.

Section 2 shows the evolution of the current systems generated by the flow bursts, while in section 3 we investigate more closely the various current systems associated with the magnetic field changes driven by an individual flow burst, which results in a more complete SCW picture. Section 4 addresses the current closure at the inner boundary, taken as a crude proxy for the ionosphere, and section 5 provides a summary and conclusions.

2. Evolution of Current Systems

As demonstrated by Figure 1, the initial flow burst near midnight is followed by additional flow bursts off midnight, leading to a somewhat turbulent accumulation of magnetic flux nearer to Earth. Each of the flow channels generates current systems involving also field-aligned currents that connect the tail with the ionosphere. First, we provide an overview of the evolution of the total region 1- and region 2-type field-aligned currents at the inner simulation boundary, shown in Figure 2. The curve for the region 1-type current (red curve) differs slightly from Figure 7b in

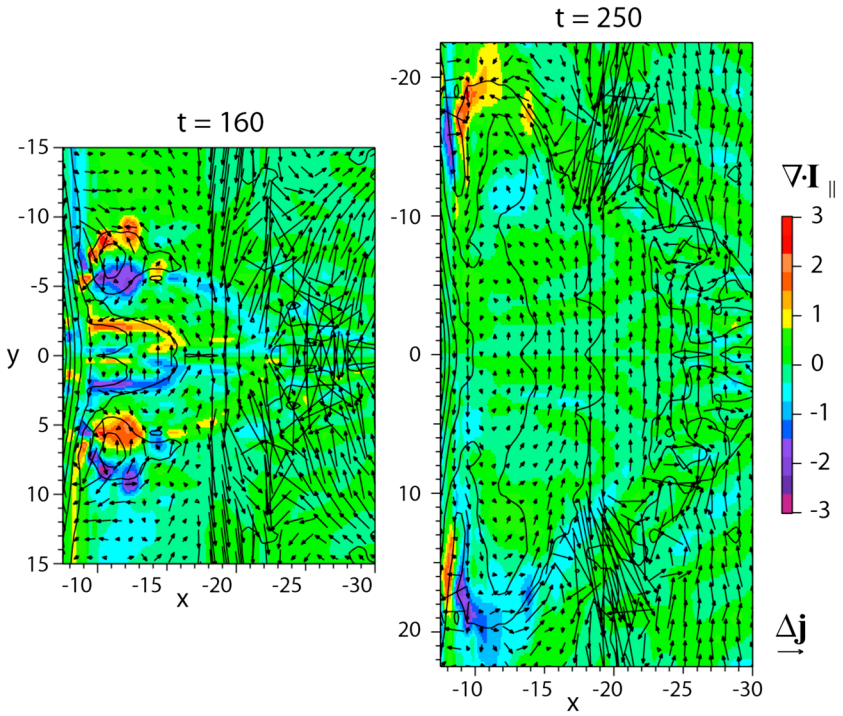

Figure 4. Color-coded divergence to field-aligned currents $\nabla \cdot \mathbf{I}_{\parallel}$, with $\mathbf{I}_{\parallel} = \int \mathbf{j}_{\parallel} dz$, together with changes of the current density vectors at $z = 0$, $\Delta\mathbf{j} = \mathbf{j} - \mathbf{j_0}$. Solid lines are contours of constant B_z at intervals of 0.5 (10 nT).

Birn and Hesse [2013], because here we included only currents within the closed field line region, whereas *Birn and Hesse* [2013] also included currents within the open (lobe) regions. Figure 2 also includes the driven phase ($30 < t < 61$, dashed lines), which already causes moderate increases in both, region 1 and region 2, systems. The integrated effects of the major flow channels at $t > 125$ and $t > 150$ are clearly visible, resulting in increases of both region 1- and region 2-type currents. The increases in region 1-type currents are about twice as large as those of the region 2 currents. We note that these currents most likely do not represent the total current closing within the ionosphere, because they may be comprised of individual "wedgelets" [*Rostoker*, 1998], which may close separately.

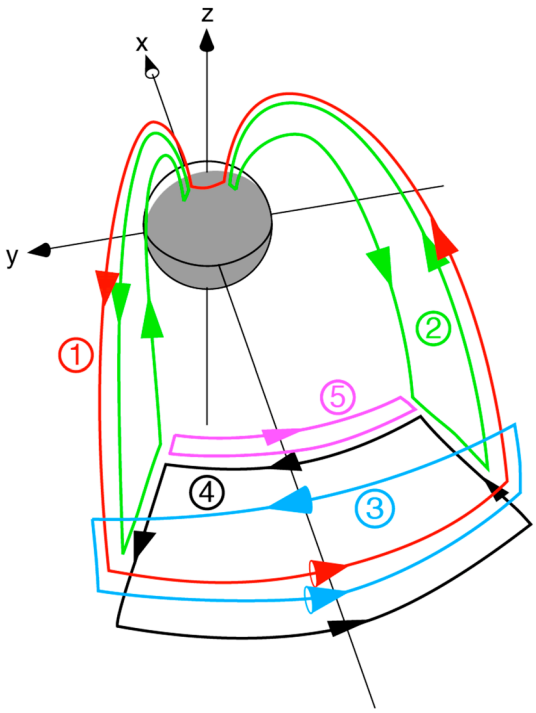

Figure 5. Schematic of major current systems contributing to the SCW, modified from Plate 4 of *Birn et al.* [1999] by the addition of loops 4 and 5; a preliminary version of this figure without loop 5 is also shown by *Kepko et al.* [2014].

Details of the field-aligned currents at the inner boundary are demonstrated by Figure 3, which shows the color-coded field-aligned current component $j_{\parallel x}$ for various times, demonstrating the effects of the initial flow burst ($t = 140$) and the two subsequent flow bursts ($t = 160$), each causing a wedgelet of region 1-type with a minor region 2-type system at lower latitude. At later times the effects of the flow bursts decrease within the expanding bulge, while the major contributions from the edges remain.

The evolution of current diversion (color coded) and the changes in the currents (vectors) in the

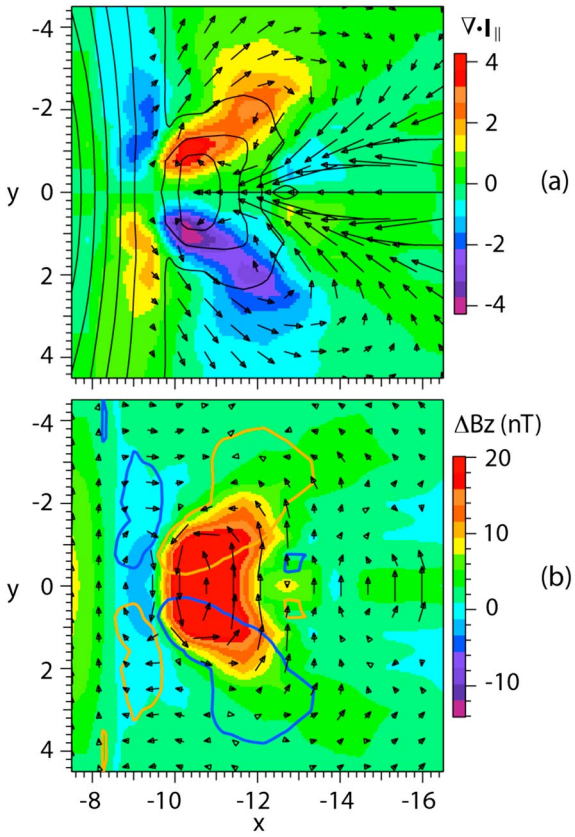

Figure 6. (a) Divergence to field-aligned currents, integrated over z (color), flow vectors, and magnetic field (B_z) contours in the equatorial plane at $t = 132$; (b) equatorial current density vectors $\Delta\mathbf{j}$ (arrows) associated with dipolarization (ΔB_z, color), indicating loops 4 and 5 in Figure 5; blue and yellow contours show the regions of main current diversion from Figure 6a.

equatorial plane are demonstrated by Figure 4. Here $\Delta\mathbf{j} = \mathbf{j} - \mathbf{j_0}$ are the changes of the current density vectors at $z = 0$, where $\mathbf{j_0}$ represents current density vectors at $t = 61$ prior to the onset of reconnection. While the effects of the initial flow burst remain near $y = 0$, the two additional flow bursts near $y = \pm 7$ (Figure 1) each sets up an additional current loop of type 4 (Figure 5) with the corresponding current diversion predominantly to region 1. However, at late times the current eddies within the inner region disintegrate, and the system appears dominated by a single wide loop of type 4.

3. Modified SCW Loop Picture

In this section we look more closely into the current systems set up by an individual flow burst. We start with a schematic of the major current systems that we found to contribute to the effects of a single flow burst. These current systems are illustrated in Figure 5, modified from *Birn et al.* [1999, Plate 4] by the addition of loops 4 and 5. (An earlier version of this figure without loop 5 is presented by *Kepko et al.* [2014]; Figure 3.) The presence of loop 4 has also been demonstrated earlier in Plate 1 of *Birn et al.* [2000].

Loop 4 is directly related to the increase of B_z near the equatorial plane, that is, the dipolarization, as demonstrated by Figure 6b, showing the changes in current density, $\Delta\mathbf{j} = \mathbf{j} - \mathbf{j_0}$ (where $\mathbf{j_0}$ again represents current density vectors at $t = 61$ prior to the onset of reconnection), superposed on the color-coded magnitude of $\Delta B_z = B_z - B_{z0}$. The top part shows the color-coded regions of current diversion $\nabla \cdot \mathbf{I}_{||}$, obtained by integrating $\nabla \cdot \mathbf{j}_{||}$ in z, together with contours of B_z and velocity vectors. The regions of current diversion are also indicated in Figure 6b by heavy blue and yellow contours.

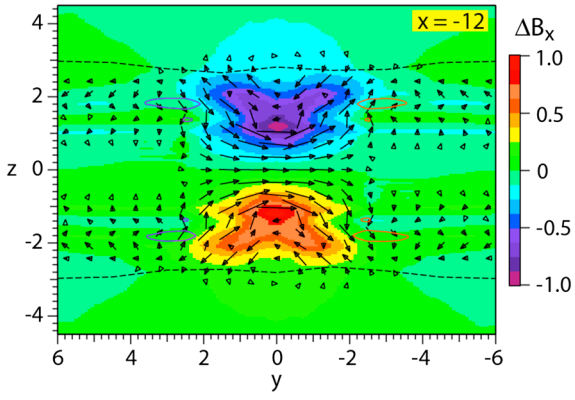

Figure 7. Changes in B_x (color) at $t = 132$ for $x = -12$, together with current density vectors ($\Delta\mathbf{j}$), related to loop 1 and 3 currents in Figure 5. The colored contours indicate the regions of enhanced parallel currents. Dashed lines show the open-closed field line boundaries.

Figure 6a shows not only the dominant diversion to region 1-type currents, resulting from the vortex flows indicated by the velocity vectors, but also a diversion to region 2-type currents earthward of it, pointed out already by *Birn and Hesse* [2013, Figure 15]. This system is set up by the flow shear earthward of the azimuthally deflected flow. Figure 6b indicates that this diversion is spatially related to current loop 5 in Figure 5 with opposite sense to loop 4, surrounding a region of slightly decreased magnitude of B_z. This region coincides with a region of enhanced pressure [*Birn and Hesse*, 2013, Figure 9] just earthward of the

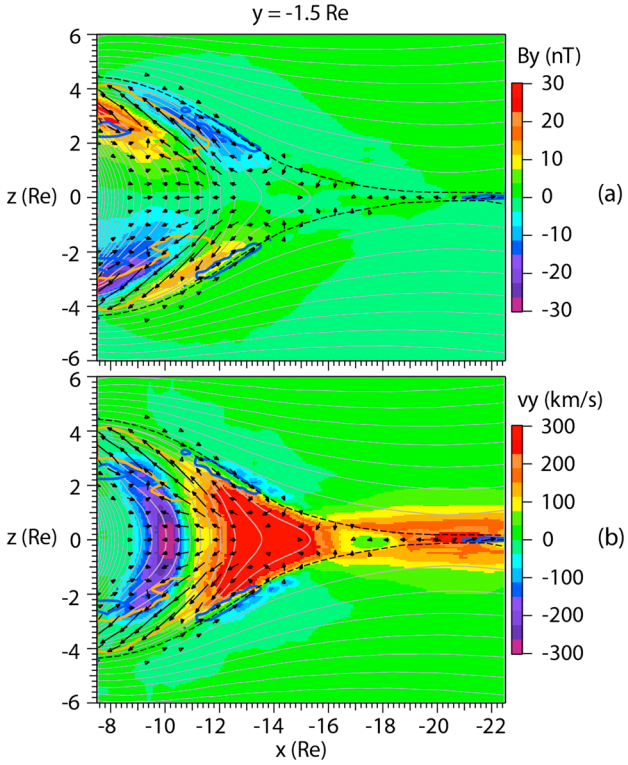

Figure 8. (a) Color-coded B_y and (b) v_y at $t = 132$ at $y = -1.5$, together with current density vectors ($\Delta\mathbf{j}$). Heavy blue and orange contours indicate regions of enhanced tailward and earthward field-aligned currents, respectively. Dashed lines show the separatrices (open-closed field line boundaries).

dipolarization front. The current diversion is related to azimuthal pressure gradients, as governed by Vasyliunas' equation [*Vasyliūnas*, 1970]

$$j_{\parallel} = -(\mathbf{B}/B) \cdot \nabla p \times \nabla V \qquad (3)$$

where $V = \int ds/B$ is the differential flux tube volume, integrated along a field line.

Another effect of the dipolarization is the decrease of $|B_x|$ at higher latitudes off the equatorial plane, demonstrated by Figure 7, which is closely related to the reduction of the total current (current disruption). This reduction is associated with loops 1 and 3. While loop 1 represents the main part of the standard SCW picture, loop 3 indicates that part of this current may close within the magnetotail, which is presumably the dominant type in Mercury's magnetosphere, where the lack of an ionosphere prevents the possibility of ionospheric current closure [*Kepko et al.*, 2014].

The additional current systems shown as loops 2 are related to the braking and diversion of flow around the Earth, which results in an increase of $|B_y|$, illustrated in Figure 8a for the dawnside by red ($z > 0$) and blue ($z < 0$) colors, surrounded by earthward current at higher latitude and tailward current at lower latitude. The connection between these currents occurs away from the equator, while near the equatorial plane the earthward currents of loop 4 dominate.

Figure 8a also shows regions of opposite B_y at higher latitudes ($-13 \le x \le -10$, $|y| \approx 3$) just inside the separatrices (dashed lines). As demonstrated by Figure 8b, these distortions of B_y result from flows toward midnight (red-orange regions), which are part of the vortices generated on the outside of an earthward flow burst (Figure 1). The distortions of B_y lead to field-aligned currents, opposite to those of region 1, but at higher latitude. In the simulation, however, these currents are mainly closed within the box and do not lead to notable field-aligned currents at the inner boundary. For simplicity, these current loops are not included in Figure 5.

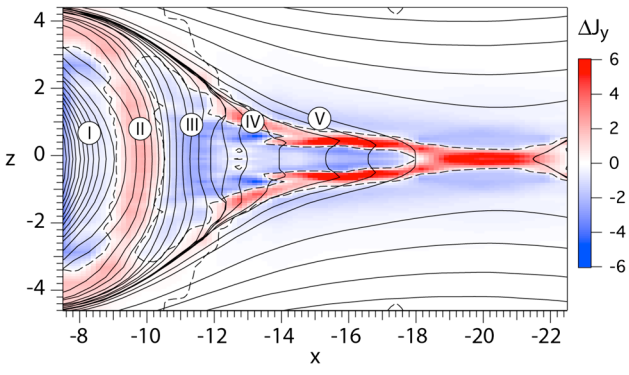

Figure 9. Color-coded current density Δj_y at $t = 132$ at $y = 0$. Red and blue colors show duskward and dawnward currents, respectively. The dashed lines emphasize the boundaries between the two directions.

All loops, except for loop 2, close through the midnight meridional plane, $y = 0$. This allows us to estimate their relative magnitude. Figure 9 shows the color-coded change in the cross-tail current density at $t = 132$, red showing duskward and blue dawnward currents. The currents are by no means "wirelike." They form layers or are even

Table 1. Magnitude of the Cross-Tail Currents in Regions I–V in Figure 9 and the Resulting Currents in Loops 1–5, Schematically Shown in Figure 5, at $t = 132$

Loop	I_I	I_{II}	I_{III}	I_{IV}	I_V	1	2	3	4	5	R1	R2
ΔI (MA)	0.31	0.51	0.69	0.59	0.47	0.37	0.21	0.12	0.20	0.31	0.58	0.21

volume-filling regions in space. The blue region earthward of $x \gtrsim -9$ (region I) corresponds to the dawnward portion of loop 5. The adjacent red region earthward of $x \gtrsim -10$ (region II) consists of the duskward parts of loops 5 and 4. The blue region further out, extending to $x \approx -18$ at $z = 0$ (region III), consists of the dawnward parts of loops 1, 3, and 4. This region is surrounded by thin red layers connected to the reconnection site (region IV), which include the duskward closure of loop 3. These layers are surrounded at larger $|z|$ by dawnward currents (blue, region V), which presumably close with parts of the underlying duskward currents. (This loop is not included in Figure 5.)

We integrated the eastward and westward currents in Figure 9 for $z > 0$ out to $x = -18$ to provide estimates of the relative magnitudes of the different loops within one hemisphere. The results are shown in Table 1. The loop 2 current was assumed to be ~60% of the loop 1 current, based on our finding that the change in total region 2 (R2)-type current at this time is about 37% of the change in region 1 (R1)-type current (comprising both loop 1 and loop 2 currents), as indicated by Figure 2. This ratio agrees well with observational results [*Sergeev et al.*, 2014].

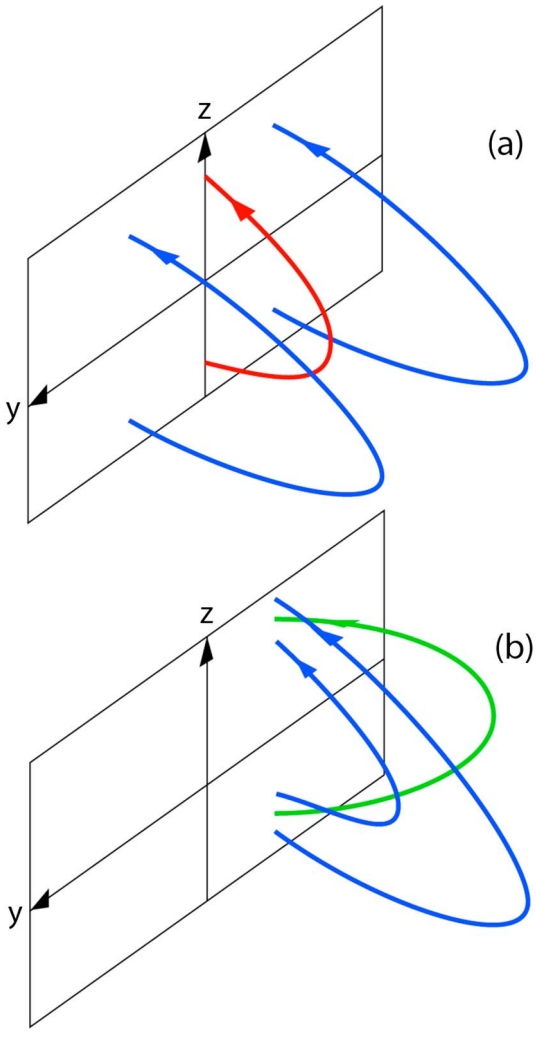

Figure 10. Magnetic distortion from (a) dipolarization and (b) azimuthal flow.

4. Ionospheric Current Closure

On the short substorm expansion time scale we might, to the lowest order, consider magnetic field lines as tied in the ionosphere, that is, treating the ionosphere as a solid, ideally conducting wall. This is equivalent to the boundary conditions imposed at the inner boundary of our simulation box. The closure of the currents at this boundary then might provide a crude proxy for the ionospheric closure. The boundary currents can be considered as surface currents associated with the perturbations of B_z and B_y across the conducting surface with

$$J_y = \int j_y dx = -(B_{z+} - B_{z-}) \tag{4}$$

where B_{z-} and B_{z+} define the values of B_z just inside and outside the inner boundary, respectively. If we assume that the value outside remains unchanged, we can identify B_{z+} with the value at the initial time, $t = 61$, and obtain

$$J_y = \Delta B_z = B_z - B_z|_{t=61} \tag{5}$$

Similarly, we find

$$J_z = \int j_z dx = (B_{y+} - B_{y-}) = -\Delta B_y \tag{6}$$

Thus, positive ΔB_z represents westward current. (Note that this corresponds to perturbations above the ionosphere.) Positive (negative) ΔB_y represents equatorward (poleward) current on the dawnside (duskside) Northern Hemisphere with opposite directions in the Southern Hemisphere.

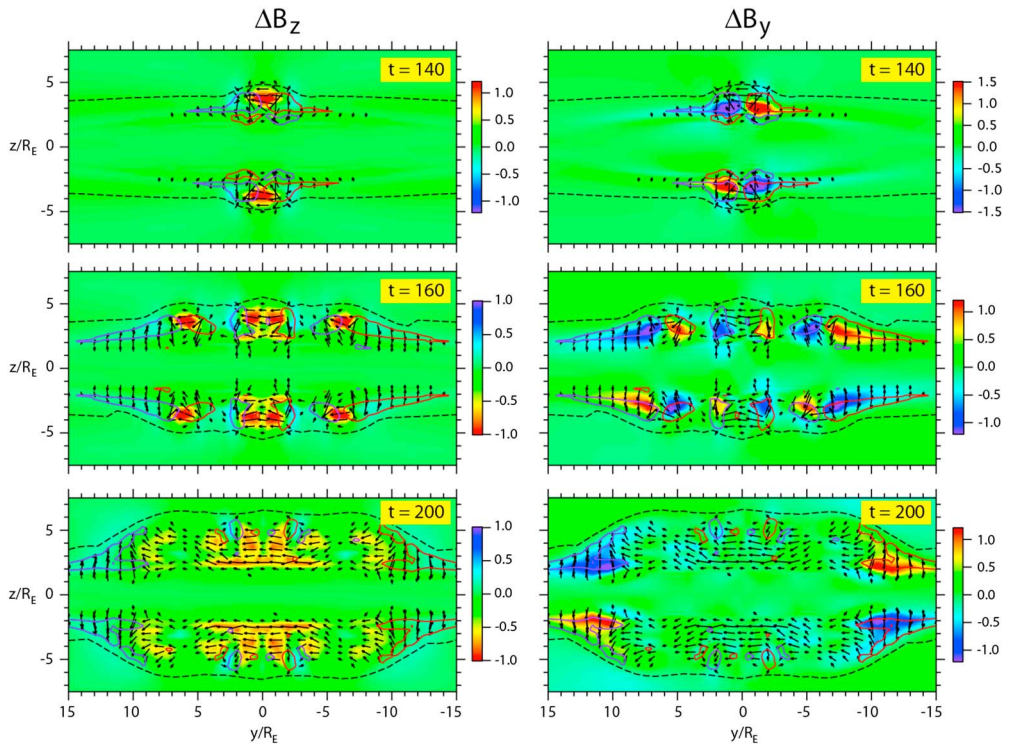

Figure 11. Magnetic perturbations, ΔB_z and ΔB_y (color), at the inner boundary for various times as indicated. Arrows indicate the surface current vectors associated with these perturbations. The colored contours indicate the regions of strong field-aligned currents $j_{\|x}$ shown in Figure 3. The dashed lines again show the open-closed field line boundaries.

The basic relationship between the magnetic field perturbations and the currents is illustrated in Figure 10. Figure 10a shows a dipolarized field line (red) between two still-stretched field lines (blue). The shear between the red and the blue lines (rotation of B_z/B_x as function of y) is the signature of the (region 1-type) field-aligned currents and the increase of B_z at the boundary indicates westward current at the foot points of the affected field lines. Figure 10b shows an azimuthally bent field line (green) between two field lines (blue) more closely aligned with the x direction. The shear between the green and the blue lines (rotation of B_y/B_x as function of z) is the signature of the field-aligned currents of region 1 signature above and region 2 signature below the distorted green field line; the increase of $|B_y|$ at the boundary indicates equatorward current at the foot points of the affected field lines.

The current closure in the simulation is demonstrated clearly by Figure 11, which shows the color-coded perturbations of the magnetic field components ΔB_z and ΔB_y, perpendicular to the magnetic field, and the associated surface current vectors (arrows) at the inner boundary for various times. Regions of strong field-aligned currents $j_{\|x}$, as shown in Figure 3, are indicated by colored contours and the open-closed boundaries by dashed lines. The perturbations ΔB_z (Figure 11, left) represent current closure through westward currents, which is part of the traditional SCW picture, whereas the perturbations ΔB_y (Figure 11, right) show the North-South closure between the region 1- and region 2-type currents. The integrated currents at $t = 140$ correspond to $\sim 2.6 \times 10^5$ A (westward) and $\sim 4.6 \times 10^5$ A (equatorward on the dawnside). It is not clear, however, to what extent this result can be transferred to ionospheric closure, because of our crude treatment of the "ionosphere" as a plane surface, neglecting finite resistance and Hall effects, which are expected to contribute to an enhanced closure through east-west currents through the "Cowling channel" [e.g., *Cowling*, 1932; *Baumjohann*, 1983; *Yoshikawa et al.*, 2013].

At $t = 160$ each of the wedgelets is associated with both types of current closures; there are only minor eastward currents between different wedgelets, whereas at later times ($t = 200$) the current distribution approaches a single wider wedge. The westward currents at this time, however, are not very uniform and spread over different latitudes. Showing the perpendicular components of ΔB_z eliminates compressional effects near $z = 0$, which are not expected to contribute to ionospheric current closure.

5. Summary and Discussion

Using a three-dimensional MHD simulation of magnetotail reconnection and dipolarization [*Birn et al.*, 2011], we have further investigated properties of current diversion associated with the substorm current wedge (SCW), extending the investigation of *Birn and Hesse* [2013]. Particular emphasis was on the current systems contributing to the SCW during various stages. In this context it is useful to distinguish the buildup of the current systems and their persistence.

In general, the buildup of the SCW can be attributed to the consequences of one or more earthward flow bursts, generated by reconnection and apparently modified by cross-tail structure associated with ballooning/interchange-type instability [*Birn et al.*, 2011]. The evolution starts with a single flow burst near midnight, followed by two flow bursts off midnight and subsequent more turbulent flows. The flow channels can be identified as low-entropy flux tubes, associated with strong enhancements of B_z (dipolarization fronts). The low-entropy, high-B_z flux tubes accumulate near Earth when the flows get stopped and diverted around Earth. Each of the flow channels distorts the magnetic field and builds up (drives) a current system akin to the standard SCW (a wedgelet) [*Rostoker*, 1998], but when the dipolarized fields accumulate near Earth the combined system eventually becomes dominated by a single wide wedge.

The distortions of the magnetic field and the associated currents persists even after the flows subside. In that case the current systems and particularly the field-aligned currents are commonly inferred from force balance [e.g., *Wolf et al.*, 2009], involving pressure gradients and gradients of the magnetic flux tube volume. Here we focused instead on the magnetic field changes, which are more easily observable than the currents and can be associated with simple current loops, supporting and complementing the standard SCW picture. The major current systems contributing to the total SCW as well as to a single wedgelet are illustrated in Figure 5, modified from *Birn et al.* [1999]. They can be attributed to localized changes in B_x, B_y, and B_z, respectively.

One main effect of a flow burst is the dipolarization, which is part of a propagating low-entropy flow channel but also part of the accumulation of deposited low-entropy flux tubes. The enhanced B_z at or near the equatorial plane is associated with current loop 4, reducing the cross-tail current farther out but increasing it closer in with radial connections at the edges of the dipolarized region. A minor modification is current loop 5, which is related to a local reduction of B_z, associated with a pressure increase earthward of a dipolarization front, with azimuthal gradients that correspond to a diversion to region 2-type currents.

A second effect of the dipolarization is the decrease of $|B_x|$ at higher latitudes, which is closely related to the reduction of the total current in that region (current disruption). This reduction is associated with loops 1 and 3. These loops contribute to the region 1-type field-aligned currents, which are part of the standard SCW. In Mercury's magnetosphere, where the lack of an ionosphere prevents the possibility of ionospheric current closure [*Kepko et al.*, 2014], they presumably close within the magnetotail (loop 3).

The third effect is the increase of $|B_y|$ resulting from the field deformation by azimuthal flows after braking and diversion. This results in the current loops 2 contributing to both region 1 on the outside and region 2 currents on the inside. The flow braking is also associated with a pressure enhancement, which provides an alternative method of inferring the region 2-type currents via equation (3) from the azimuthal pressure gradients. This result is consistent with Time History of Events and Macroscale Interactions during Substorm (THEMIS) observations [*Dubyagin et al.*, 2010].

The currents in loop 4 in Figure 5 appear to be unrelated to the wedge currents. However, a different view arises when the currents of Figure 5 are combined, disregarding loops 3 and 5, which are confined to the tail. In that case we obtain the two basic loops of Figure 12, equivalent to Figure 1b of *Sergeev et al.* [2014]. Part of the loop 4 currents now contribute to the region 1 currents, while the earthward portion becomes part of the region 2 loop. We note, however, that the region 1 and 2 loops are not separated but may be connected through radial tail currents (Figure 12, dashed lines). These currents were found to change direction between the vicinity of the equatorial plane, where they are part of loop 4 and higher latitudes, where they are part of loop 3. At $t = 132$ we found that these radial currents are comparable in magnitude.

Using the magnitudes of the westward and eastward currents at $y = 0$, we estimated the magnitudes of the different current loops in Figure 5 at the time $t = 132$, just after the buildup of the SCW from the first flow burst. We found that they are similar in magnitude, with 0.36, 0.36, 0.16, 0.20, and 0.31 MA for loops

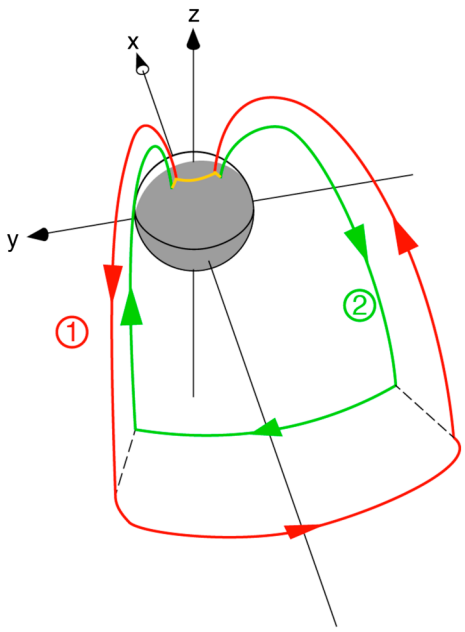

Figure 12. Schematic of current systems contributing to the SCW.

1–5, respectively. They are not wirelike but rather distributed in sheets or even filling larger space volumes. We stress that, in estimating the currents of loops 1 and 2 (or R1 and R2) from the change in cross-tail currents, it is important to include the locally closed currents. Using the total eastward and westward current perturbations in the tail may lead to an overestimate of region 1 and 2 currents.

We also investigated the current closure at the inner boundary, taken as a crude proxy of an idealized ionosphere. We demonstrated the closure of the region 1-type wedge currents through westward currents, as postulated in the original SCW picture [*McPherron et al.*, 1973], as well as the closure between the region 1- and region 2-type currents by North-South currents. Surprisingly, in a single wedge, the N-S currents were larger than the westward currents by a factor of almost 2. However, this result should be applied with caution to the ionosphere because of our crude approximation as a solid plane slab, neglecting finite resistance and Hall effects. In particular, the Cowling effect [e.g., *Cowling*, 1932; *Baumjohann*, 1983; *Yoshikawa et al.*, 2013] should contribute to an enhanced closure through EW currents.

We should add cautionary remarks on the representation of plasma dynamics by current loops. First of all, as demonstrated here, the representation is not unique. Current loops may be combined in different ways. If current lines are followed in a simulation (in real space that is not possible), they typically do not close in themselves, so investigating current closure may lead one astray, and it depends strongly on whether total currents or current perturbations are followed. Finally, none of the representations necessarily implies that changing the current in one part of a loop causes a change in the rest of the loop. In a plasma a local change in the current may just lead to local closure currents without affecting the global system [*Birn et al.*, 2000].

The association of current loops with particular magnetic field changes provides a better picture of cause and effect and of the interconnection between the systems. A major role in the substorm dynamics is played by the dipolarization in the tail, which includes both an increase of B_z in a local equatorial region as well as a decrease of $|B_x|$ away from the equator, related to current loops 4 and 1 (and 3) constituting the major (region 1-type) part of the SCW. The additional region 2-type currents are related to two effects, the buildup by the azimuthal flow diversion causing increases in $|B_y|$, which also contributes to region 1-type currents, and a maintenance by the local increase of pressure (associated with a decrease of B_z and current loop 5), earthward of the dipolarized region. All of these effects are consequences of the plasma and field dynamics, particularly through plasma flows, their braking and diversion, and hence strongly coupled.

The association of currents with magnetic field changes also brings the modified SCW model closer to observations, which are based on magnetic fields rather than currents. The necessity of adding a R2 current loop was demonstrated recently by *Sergeev et al.* [2011, 2014], using Cluster and THEMIS observations in connection with geosynchronous observations. The radial width of the westward current associated with this loop of $\sim 1\, R_E$ also agrees well the width inferred from observations [*Sergeev et al.*, 2014]. However, our results differ from the two-loop R1/R2 model of Sergeev et al. [*Sergeev et al.*, 2011, 2014] by two aspects. The westward current in the localized region II (Figure 9) is not necessarily equal to the R2 field-aligned currents, due to the presence of loops 4 and 5, which lead to an increase of the westward currents, and loop 2, which causes a reduction by radial currents connected to R1 currents. Similarly, the eastward current perturbations associated with R1 currents are enhanced by the local loop 3 and 4 currents but reduced by loop 2. The effects of loop 3 disappear if the cross-tail currents are evaluated from lobe magnetic fields but the effects of radial connection with the R2 loop remain. Hence, the R1 and R2 loops inferred by *Sergeev et al.* [2011, 2014] are not necessarily distinct but may be connected through radial currents and modified through local current loops.

Acknowledgments
This work was performed mostly at Los Alamos National Laboratory under a Guest Scientist agreement, supported by NASA grants NNX13AD10G and NNX13AD21G and NSF grant 1203711. J.B. also acknowledges the hospitality and support of the International Space Science Institute, Bern, Switzerland, and fruitful discussions with Wolfgang Baumjohann and members of the ISSI team on the substorm current wedge. Data necessary to understand, evaluate, replicate, and build upon the reported research will be made available upon request.

Michael Liemohn thanks Emma Woodfield and an anonymous reviewer for their assistance in evaluating this paper.

References

Baumjohann, W. (1983), Ionospheric and field-aligned current systems in the auroral zone: A concise review, *Adv. Space Res.*, *2*, 55–62.
Birn, J., and M. Hesse (2013), The substorm current wedge in MHD simulations, *J. Geophys. Res. Space Physics*, *118*, 3364–3376, doi:10.1002/jgra.50187.
Birn, J., M. Hesse, G. Haerendel, W. Baumjohann, and K. Shiokawa (1999), Flow braking and the substorm current wedge, *J. Geophys. Res.*, *104*, 19,895–19,903.
Birn, J., J. T. Gosling, M. Hesse, T. G. Forbes, and E. R. Priest (2000), Simulations of three-dimensional reconnection in the solar corona, *Astrophys. J.*, *541*, 1078–1095.
Birn, J., M. Hesse, K. Schindler, and S. Zaharia (2009), Role of entropy in magnetotail dynamics, *J. Geophys. Res.*, *114*, A00D03, doi:10.1029/2008JA014015.
Birn, J., R. Nakamura, E. V. Panov, and M. Hesse (2011), Bursty bulk flows and dipolarization in MHD simulations of magnetotail reconnection, *J. Geophys. Res.*, *116*, A01210, doi:10.1029/2010JA016083.
Cowling, T. G. (1932), The electrical conductivity of an ionised gas in the presence of a magnetic field, *Mon. Not. R. Astron. Soc.*, *93*, 90–98.
Dubyagin, S., V. Sergeev, S. Apatenkov, V. Angelopoulos, R. Nakamura, J. McFadden, D. Larson, and J. Bonnell (2010), Pressure and entropy changes in the flow-braking region during magnetic field dipolarization, *J. Geophys. Res.*, *115*, A10225, doi:10.1029/2010JA015625.
Henderson, M. G., G. D. Reeves, and J. S. Murphree (1998), Are north-south aligned auroral structures an ionospheric manifestation of bursty bulk flows?, *Geophys. Res. Lett.*, *25*, 3737–3740.
Hesse, M., and J. Birn (1993), Three-dimensional magnetotail equilibria by numerical relaxation techniques, *J. Geophys. Res.*, *98*, 3973–3982.
Iijima, T., and T. A. Potemra (1976), The amplitude distribution of field-aligned currents at northern high latitudes observed by Triad, *J. Geophys. Res.*, *81*, 2165–2174.
Kepko, L., K.-H. Glaßmeier, J. Slavin, and T. Sundberg (2014), The substorm current wedge at Mercury and Earth, in *Magnetotails in the Solar System, Geophys. Monogr. Ser.*, edited by A. Keiling, Washington, D. C., in press.
Lyons, L. R., T. Nagai, G. T. Blanchard, J. C. Samson, T. Yamamoto, T. Mukai, A. Nishida, and S. Kokubun (1999), Association between Geotail plasma flows and auroral poleward boundary intensifications observed by CANOPUS photometers, *J. Geophys. Res.*, *104*, 4485–4500.
McPherron, R. L., C. T. Russell, and M. P. Aubry (1973), Satellite studies of magnetospheric substorms on August 15, 1968: 9. Phenomenological model for substorms, *J. Geophys. Res.*, *78*, 3131–3149.
Nakamura, R., W. Baumjohann, M. Brittnacher, V. A. Sergeev, M. Kubyshkina, T. Mukai, and K. Liou (2001a), Flow bursts and auroral activations: Onset timing and foot point location, *J. Geophys. Res.*, *106*, 10,777–10,789.
Nakamura, R., W. Baumjohann, R. Schödel, M. Brittnacher, V. A. Sergeev, M. Kubyshkina, T. Mukai, and K. Liou (2001b), Earthward flow bursts, auroral streamers, and small expansions, *J. Geophys. Res.*, *106*, 10,791–10,802.
Rostoker, G. (1998), On the place of the pseudo-breakup in a magnetospheric substorm, *Geophys. Res. Lett.*, *25*, 217–220.
Sergeev, V. A., K. Liou, C.-I. Meng, P. T. Newell, M. Brittnacher, G. Parks, and G. D. Reeves (1999), Development of auroral streamers in association with localized impulsive injections to the inner magnetotail, *Geophys. Res. Lett.*, *26*, 417–420.
Sergeev, V. A., N. A. Tsyganenko, M. V. Smirnov, A. V. Nikolaev, H. J. Singer, and W. Baumjohann (2011), Magnetic effects of the substorm current wedge in a "spread-out wire" model and their comparison with ground, geosynchronous, and tail lobe data, *J. Geophys. Res.*, *116*, A07218, doi:10.1029/2011JA016471.
Sergeev, V. A., A. V. Nikolaev, N. A. Tsyganenko, V. Angelopoulos, A. V. Runov, H. J. Singer, and J. Yang (2014), Testing a two-loop pattern of the substorm current wedge (SCW2L), *J. Geophys. Res. Space Physics*, *119*, 947–963, doi:10.1002/2013JA019629.
Vasyliūnas, V. M. (1970), Mathematical models of magnetospheric convection and its coupling to the ionosphere, in *Particles and Fields in the Magnetosphere*, edited by B. M. McCormac, p. 60, D. Reidel, Norwell, Mass.
Wolf, R. A., Y. Wan, X. Xing, J.-C. Zhang, and S. Sazykin (2009), Entropy and plasma sheet transport, *J. Geophys. Res.*, *114*, A00D05, doi:10.1029/2009JA014044.
Yoshikawa, A., O. Amm, H. Vanhamäki, A. Nakamizo, and R. Fujii (2013), Theory of Cowling channel formation by reflection of shear Alfven waves from the auroral ionosphere, *J. Geophys. Res. Space Physics*, *118*, 6416–6425, doi:10.1002/jgra.50514.